Insights into the effect of cobalt substitution into copper-manganese oxides on enhanced benzene oxidation activity

Siyu Ding [a], Chen Zhu [a], Hajime Hojo [b], Hisahiro Einaga [b,*]

[a] *Department of Molecular and Material Sciences, Interdisciplinary Graduate School of Engineering Sciences, Kyushu University, 6-1, Kasugakoen, Kasuga, Fukuoka 816-8580, Japan*

[b] *Department of Advanced Materials Science and Engineering, Faculty of Engineering Sciences, Kyushu University, 6-1, Kasugakoen, Kasuga, Fukuoka 816-8580, Japan*

ARTICLE INFO

ABSTRACT

Co-substituted Cu-Mn spinel oxides were synthesized, characterized, and catalytic performance for benzene oxidation was evaluated. Spinel phases, and the substitution of Mn sites by Co were confirmed for the ternary oxides. $Co_{0.2}Cu_{0.8}MnO_y$ showed the highest activities with the lowest apparent activation energy among the ternary oxides. The improved catalytic properties due to Co substitution are attributed to more activated lattice oxygen, stronger adsorption of benzene, and a larger specific surface area. Density functional theory simulations also revealed that the Co substitution enhanced the reactivity of the lattice oxygen. Adsorbed and activated benzene reacted with lattice oxygen to form abundant oxygen defects, which promoted O_2 adsorption and dissociation, contributing to enhanced catalytic activity. The effect of water vapor on the catalytic benzene oxidation was also clarified.

1. Introduction

Volatile organic compounds (VOCs) emitted from products, industrial processes, and vehicles are harmful to human health and the environment, and the advancement of technologies to remove them remains important [1–3]. Among the VOC treatment technology, including catalytic oxidation, biodegradation, and adsorption, the catalytic oxidation process can be used under wide conditions [4–6]. It can remove VOCs with high efficiency, selectivity, and low-temperature activity with some catalysts and has been widely used in industrial pollution control. Supported nooble metal (Pt, Pd, Au) catalysts are known to be active for VOCs degradation; however, the high price, susceptible poisoning by chlorine or sulfur compounds, and low water resistance limit their applications [7–10]. For economic considerations, transition metal oxides with activity comparable to noble metals are preferred for further applications. Single transition metal oxides, including MnO_2 [11–13], Co_3O_4 [14–16], Fe_2O_3 [16], CuO [17], and CeO_2 [18,19] have been investigated for the removal of various pollutants, including benzene, toluene, formaldehyde, and CO. Moreover, composite oxides such as Cu–Mn [20–22], Mn–Co [23,24], Ni-Co [25], Mn–Ce [26–28], Co–Ce [29–31], Ce-Zr [32], and Ce–Sn [33] have high catalytic properties due to charge transfer redox pairing, increased

surface area, and high lattice oxygen activity.

Previous studies have reported that Cu-Mn spinel-type binary oxides have higher CO oxidation efficiency than single oxides, indicating that spinel-structured compounds may be a potential alternative for precious metal catalysts [34]. Furthermore, more active catalysts are desired to oxidize less reactive aromatic compounds. Doping with other elements is a productive approach to enhance the catalytic properties by creating a highly active surface, improving the charge transfer by various metal ions existing in one crystal structure, and enhancing the reactivity of oxygen species [36]. For instance, Hu et al. investigated the oxidation of phenolic compounds on K-OMS-2 nanofibers doped with transition metal ions (Cu^{2+}, Co^{3+}, and Ce^{4+}). They found that Co^{3+}-doped OMS-2 catalysts showed the highest activity for phenol removal due to the higher surface area, more oxygen vacancies, and more surface-bonded OH groups compared with undoped OMS-2 [37]. Dutta et al. discussed the hydride transfer phenomenon facilitated by cobalt-doped CuO nanoparticles, in which the stability of CuO was improved by Co doping [38]. Cobalt doped in the Mn-Ce system induced the formation of a solid solution with more active oxygen, showing excellent low-temperature oxidation of benzene [39]. Ioannides et al. reported that Cu^{2+} doped CeO_2 mixed oxides exhibited higher surface areas than the corresponding pure oxides and are efficient for the destruction of ethanol and

---

* Corresponding author.
E-mail address: einaga.hisahiro.399@m.kyushu-u.ac.jp (H. Einaga).

ethyl acetate with minimal formation of undesired byproducts (acetaldehyde) [26]. 2 % V^{5+} doped hollandite-type manganese oxide had greatly enhanced catalytic activities (1.5 times) in low-temperature oxidation of formaldehyde and high-temperature oxidation of methane by increased surface defect sites [40]. Thus, the catalytic performance was further improved by substituting the metal in the oxide with another transition metal species. Co is one of the most promising candidates for improving oxide catalyst properties.

In this study, we carried out the catalytic oxidation of benzene over Co-substituted Cu-Mn mixed oxides to investigate the effect of Co substitution on the catalyst structure, textural properties, catalytic activities, and water vapor resistance in detail. Our experimental study clarified that the Co substitution enhanced the catalytic activity of Cu-Mn spinel oxides for benzene oxidation due to the improved benzene adsorption ability, enhanced reactivity of lattice oxygen, and promoted catalyst reoxidation. Theoretical calculations (DFT) were also performed to reveal the role of substituted Co in enhanced catalytic oxidation.

2. Experimental

2.1. Catalyst preparation

The samples were synthesized by the evaporation to dry and auto-combustion method [36]. 5 mmol $Cu(NO_3)_2 \cdot 3H_2O$, $Mn(NO_3)_3 \cdot 6H_2O$ (Wako Pure Chemical, > 99.9 %), and 10 mmol citric acid (Wako Pure Chemical, 99.5 %) were dissolved in 50 mL pure water at 70 ℃ to form precursor solution, where citric acid was used as the complexing. Then, 0.1 mol/L ammonia solution was dropwise added to the precursor until the pH reached 3, continuously stirring until the solution evaporated to dryness. After drying for 24 h, the precursors auto-combusted and transferred into fluffy powders. Finally, the products were ground and then calcined at 400 ℃ for 5 h to obtain the catalysts. The Co-doped samples were prepared with corresponding atomic ratios under identical conditions. The Cu-, Mn-, Co-single oxides and $CoMn_2O_4$ mixed oxide were prepared by the same processes.

2.2. Catalytic reactions

Benzene oxidation reactions were performed with a continuous flow fixed-bed system. All the reactions were carried out with 0.1 g catalyst placed in the center pipe of a triple-tube quartz reactor in the cylindrical furnace. Reaction conditions: benzene (400 ppm, N_2 balance)-20 % O_2 was fed into the reactor with a total gas flow rate of 100 mL min^{-1}, equivalent to a weight hourly space velocity (WHSV) of 60,000 mL g^{-1} h^{-1}. The concentrations of benzene and CO_2 were measured by an FTIR spectrometer equipped with a gas cell (optical path length: 2.4 m). In the reactions with water vapor, 20 vol% of H_2O was introduced into the reactor. The water vapor concentration was measured by a dew point meter (OptiSonde General Eastern).

The benzene conversion was calculated according to the equation:

$$\text{Benzene conversion, X\%} = \frac{[C6H6]_{in} - [C6H6]_{out}}{[C6H6]_{in}} \times 100\% \qquad (1)$$

2.3. Characterization

X-ray diffraction (XRD) was taken under an Ultima IV diffractometer (RIGAKU, Japan) using Cu-Kα radiation (0.154 nm) at 40 kV, 40 mA. Scanning electron microscopy (SEM) images were observed by Helios Hydra CX (Thermo Fisher Scientific Inc., America). The specific surface area was estimated by the Brunauer-Emmett-Teller (BET) method from N_2 adsorption-desorption isotherms obtained using a BELSORP-mini II apparatus (MicrotracBEL Corp., Japan) at 77 K. Temperature-programming reduction with H_2 (H_2-TPR) experiments was carried out on a flow-type BELCAT-30 chemisorption analyzer (BEL Japan, Inc). The samples were pretreated at 600 ℃ for 1 h in an O_2 stream, and then

the measurements were performed in the range of 50–850 ℃ in 5 % H_2-N_2 with a flow rate of 30 mL min^{-1} and a temperature ramp of 5 ℃ min^{-1}.

X-ray absorption fine structure (XAFS) spectra, including extended X-ray absorption fine structure (EXAFS) and X-ray absorption near edge structure (XANES), were collected in the transmission mode using the Kyushu University beamline (KU BL06) with the storage ring energy of 1.4 GeV in the Kyushu Synchrotron Light Research Center (SAGA-LS, Japan). XANES spectra were background subtracted, edge height normalized, and then the first-order derivatives were obtained to compare the adsorption edge energies using Athena [41]. EXAFS signals (k • χ(k)) were extracted, and k^3-weighted EXAFS were Fourier transformed (FT) to R space for the Mn (6539 eV), Cu (8979 eV), and Co (7709 eV) K-edge spectra in the range of 3.0–14 Å^{-1}.

For XAFS spectra analysis, EXAFS curve fitting was performed using Artemis [41]. Phase shift and backscattering amplitude functions were calculated according to the FEFF8 code [42,43]. Wavelet transformation (WT) of the k^3-weighted EXAFS signals using a Morlet wavelet (Eq. (2)), calculated by the HAMA Fortran code [44,45]. The parameter κ represented the frequency of sine waves while σ was the Gaussian standard deviation. For a good resolution of the WT, σ was set up to 1, and the κ-value was determined by ΔR (κ = 2ΔR).

$$\Psi(t) = \frac{1}{\sqrt{2\pi}\sigma}(e^{i\kappa t} - e^{-\frac{\kappa^2\sigma^2}{2}})e^{-\frac{t^2}{2\sigma^2}} \qquad (2)$$

2.4. In situ FTIR measurements

In situ Fourier transformed infrared spectroscopy was conducted on the FT/IR-4100 (JASCO Co., Japan) equipped with a diffuse reflectance cell. First, the catalyst was pretreated in O_2 for 10 min and N_2 for 20 min at 300 ℃ with a gas flow rate of 30 mL min^{-1} to remove the impurities on the surface, and then cooled down to 150 ℃. The background spectrum was collected in the N_2 stream, and a 500 ppm benzene-N_2 balance gas with the flow rate of 30 mL min^{-1} was fed to the sample cell at 150 ℃ for 60 min, and the spectra were recorded. Then, the weakly adsorbed benzene was removed by N_2 purging for 1 h; subsequently, 20 % O_2/N_2 was introduced to investigate the reactivity of pre-adsorbed benzene at 150 °C.

2.5. Theoretical calculation method

All the calculations were carried out by periodic plane-wave first-principles density functional theory (DFT) as implemented in Vienna Ab-initio Simulations Package (VASP) with projector augmented wave (PAW) [46]. The Perdew-Burke-Ernzerhof (PBE) of functional in the generalized gradient approximation (GGA) scheme was carried to the electronic structure calculation with plane-wave truncation energy of 450 eV [47]. DFT + D3 scheme by Grimme was employed to account for the effect of Van der Waals force interaction [48]. The geometry optimization and self-consistent field (SCF) convergence criterion were set to 0.05 eV/Å and 10^{-5} eV, respectively.

The spinel $Cu_{1.5}Mn_{1.5}O_4$ (100) surface was constructed in a p (2 ×2) periodic unit cell (a = 16.674 Å, b = 16.674 Å, and c = 21.238 Å) with eight atomic layers and the bottom four layers were fixed while the top four layers were fully relaxed. 13 Å of vacuum space in the Z-direction was placed above the surface to avoid the interaction between the replicas of the slab model. A (1 × 1 × 1) Monkhorst-Pack k-point grid was applied for Brillouin zone integration. The optimized surfaces with single, dual, and triple Co substitution were denoted Co_1: CuMn(100), Co_2: CuMn(100), and Co_3: CuMn(100).

The formation energy of oxygen vacancy can be defined as:

$$E_{Vo} = E_{slab-O} - E_{slab} + 1/2\ Eo_2 \qquad (3)$$

here, E_{slab-O} is the energy of the system with one oxygen atom loss, E_{slab} is the energy of the slab, and Eo_2 is the energy of the O_2 molecule in the

gas phase [49].

The adsorption energies (E_{ads}) of benzene on the surface and O_2 on V_O were calculated by the following equation:

$$E_{ads} = E_{adsorbate-slab} - (E_{slab} + E_{adsorbate}) \qquad (4)$$

where $E_{adsorbate-slab}$, E_{slab}, and $E_{adsorbate}$ represent the energy of the adsorption system, the optimized surface, and the isolated benzene and O_2 molecule, respectively. In all adsorbate calculations, the adsorbed molecules were free to relax unconstrainedly during energy minimization to obtain the lowest-energy adsorption structures.

3. Results and discussion

3.1. Structural and textural properties

Fig. 1 shows the X-ray diffraction spectra of the catalysts. The typical Cu-Mn spinel phases ($Cu_{1.5}Mn_{1.5}O_4$ or $CuMn_2O_4$) were detected in pristine and doped samples. Diffraction peaks corresponding to CuO were also observed, and the peak intensities decreased with the decreased concentration of Cu species. No additional peaks such as CoO and Co_2O_3 were generated for the Co-containing catalysts, indicating Co species were well dispersed or incorporated into the crystal structure. The main peaks assigned to the spinel phase (Fig. 1b) progressively shifted towards higher angles while the peak corresponding to CuO did not change with increasing Co/Cu ratio, suggesting distortions in the crystalline structure or modification in the crystal aspect ratio [50]. According to the crystal radius of the metal ions listed in Table S1, the radii of Co ions were quite close to the sizes of Cu^{2+} and Mn^{3+}, and it was very likely that the insertion of Co into the Cu-Mn spinel framework led to the decrease in the lattice constant. Table 1 summarizes the specific surface area (S_{BET}), pore size distribution (D_p), and pore volume (V_p) obtained from N_2 adsorption-desorption isotherms (Fig. S1). The S_{BET} and V_p of the Co-substituted samples were larger than Cu-Mn oxides. They all showed mesoporous structures (IV-type isotherm and H3-type hysteresis), with an average size distribution of 2–5 nm. SEM images of the catalysts shown in Fig. S2 also revealed the porous structures composed of nanoparticles of 30–50 nm. Elemental mapping revealed that Cu, Mn and Co species were uniformly distributed on the catalyst surface.

To investigate the local environment of constituent metals in the Cu-

Table 1
Textural properties of the catalysts.

$Co_xCu_{1-x}MnO_y$	S_{BET}/m^2 g^{-1}	$D_p/$ nm	V_p/cm^3 g^{-1}	H_2 consumption/ mmol g^{-1}	
				50–225 °C	225–850 °C
Co_0	27.7	5.45	0.174	2.65	8.98
$Co_{0.2}$	56.8	3.50	0.256	3.11	8.33
$Co_{0.4}$	46.0	4.74	0.206	3.19	8.73
$Co_{0.5}$	57.7	3.22	0.238	2.57	9.53
$Co_{0.6}$	65.5	3.22	0.250	2.66	10.51
$Co_{0.8}$	72.4	2.83	0.228	1.93	9.51

Mn and Co-Cu-Mn spinel phases, the catalysts were characterized by X-ray absorption fine structure (XAFS) spectroscopy. Fig. 2 shows the phase-uncorrected (pu) Fourier transformed EXAFS spectra of all the catalysts reflecting the local coordination environment of Cu, Mn, and Co species, and Tables 2 and 3 summarize the detailed curve-fitting results. For pristine $CuMnO_x$, the peaks were fitted well with the Cu–Mn, Cu–Cu, and Mn–Mn single scattering paths in the $Cu_2[Mn_3Cu]O_8$ ($Cu_{1.5}Mn_{1.5}O_4$) spinel oxide, which was similar to the Cu-Mn oxides prepared by TMAH and sol-gel method in our previous works [34,35]. For $Co_{0.2}Cu_{0.8}MnO_y$, in the Cu K-edge spectra (Fig. 2a), no significant changes were observed for Cu–O in the first coordination shell; however, in the second shell, the peak at 2.56 Å was mainly ascribed to Cu–Co and Cu–Mn, and the peak at 3.01 Å was fitted well with a Cu–Cu single scattering paths (Table 2). Regarding the Mn K-edge spectra (Fig. 2b), the environment of atoms around Mn also changed, and the Mn–Co contributions were revealed (Table 3). Fig. 2c shows the Co K-edge spectra; for the reference sample Co_3O_4, the peaks were observed at 1.54, 2.52, and 2.98 Å, corresponding to Co-O, Co-Co, Co-Co, and Co-O contributions [51], respectively. After the Co substitution, the peak (2.98 Å) due to Co-Co, and Co-O contributions shifted to a higher length of 3.06 Å, indicating the Co and Cu/Mn atoms occupied the same sites. The peak positions were quite close with the increasing Co ratio, but the intensities changed, indicating the change in coordination number or the structural disorder [52].

To gain insight into the structural change, wavelet transformation (WT) of EXAFS data was performed (Fig. S3). For Co K-edge spectra of Co_3O_4 in Fig. S3c1, there were two main lobes within the R range of 2–3 Å centered at (6 Å^{-1}, 2.5 Å) and (12 Å^{-1}, 2.5 Å), associated with the

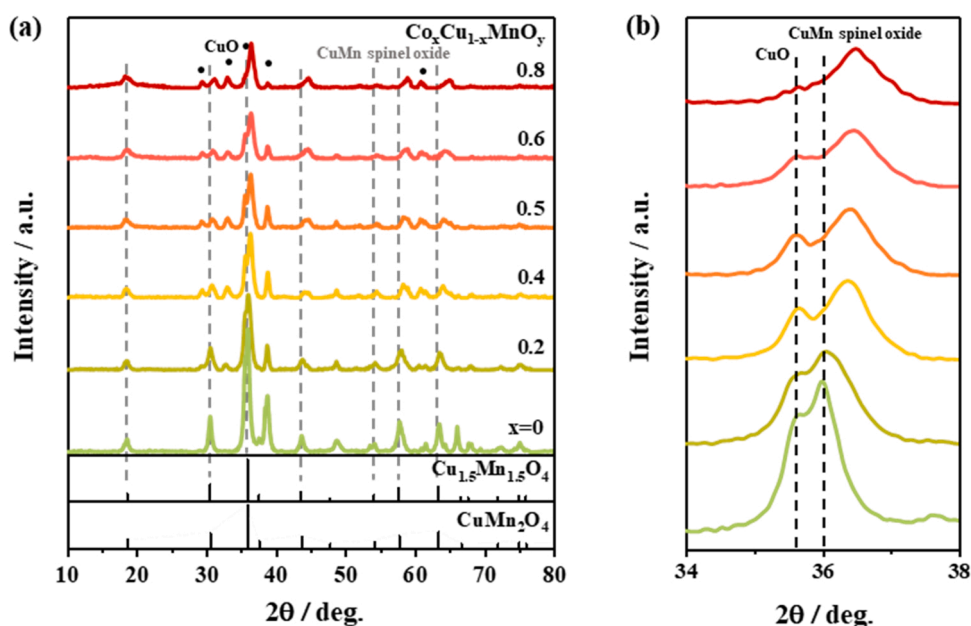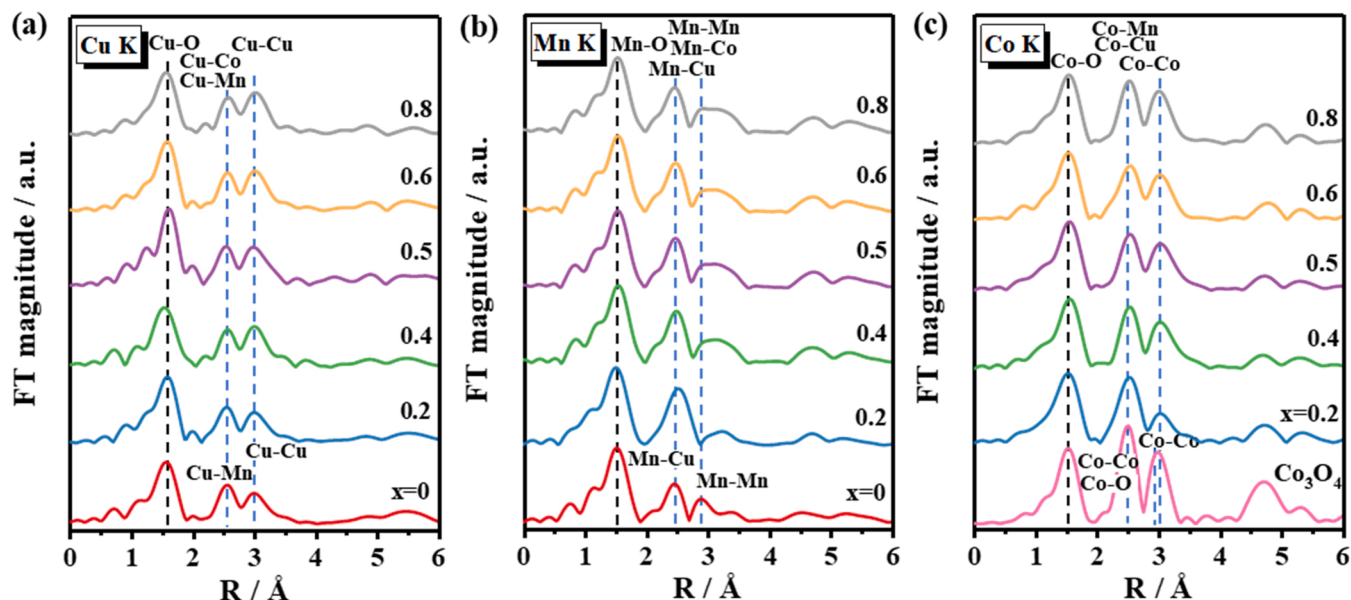**Fig. 1.** XRD spectra of the samples.

Fig. 2. Fourier transformation of k^3-weighted EXAFS spectra of $Co_xCu_{1-x}MnO_y$.

Table 2

[a]Cu K-edge EXAFS curve-fitting results.

Catalyst	Shell	CN	R/Å	$\sigma/\times 10^{-3}$ Å^2	ΔE/ eV	[b]Rf/ %
CuMn	Cu–O	3.29 ± 0.34	1.963 (0.01)	5.63	5.54	1.8
	Cu–Mn	1.65 ± 0.17	2.909 (0.06)	7.13		
	Cu–Cu	4.94 ± 0.51	3.413 (0.03)	9.11		
$Co_{0.2}Cu_{0.8}Mn$	Cu–O	3.01 ± 0.16	1.963 (0.01)	4.85	4.45	0.9
	Cu–Mn	0.92 ± 0.02	2.887 (− 0.03)	6.56		
	Cu–Co	1.53 ± 0.03	2.929 (0.01)	6.56		
	Cu–Cu	4.21 ± 0.11	3.417 (− 0.03)	5.45		

[a] The maximum number of free parameters estimated by Nyquist theorem, n = $(2\Delta k \Delta r/p)$ + 1.

[b] Residual factor, $R_f = \dfrac{\sum \left\{ k^3\chi(k)_{obs} - k^3\chi(k)_{calc} \right\}^2}{\sum \left\{ k^3 \right\} \chi(k)^2} \times 100\,\%.$

Table 3

[a]Mn K-edge EXAFS curve-fitting results.

Catalyst	Shell	CN	R/Å	$\sigma/\times 10^{-3}$ Å^2	ΔE/ eV	[b]Rf/ %
CuMn	Mn–O	4.10 ± 0.30	1.913 (− 0.01)	4.92	-2.85	3.1
	Mn–Cu	1.25 ± 0.15	2.879 (0.02)	4.10		
	Mn–Mn	2.44 ± 0.21	3.973 (0.02)	7.52		
$Co_{0.2}Cu_{0.8}Mn$	Mn–O	4.01 ± 0.06	1.963 (0.01)	3.45	-4.62	0.7
	Mn–Cu	1.76 ± 0.10	2.887 (− 0.01)	5.61		
	Mn–Co	3.47 ± 0.05	2.823 (0.02)	4.44		
	Mn–Mn	2.21 ± 0.01	3.007 (− 0.02)	1.53		

[a] The maximum number of free parameters estimated by Nyquist theorem, n = $(2\Delta k \Delta r/p)$+ 1.

[b] Residual factor, $R_f = \dfrac{\sum \left\{ k^3\chi(k)_{obs} - k^3\chi(k)_{calc} \right\}^2}{\sum \left\{ k^3 \right\} \chi(k)^2} \times 100\,\%.$

contributions of Co-O and Co-Co. However, for the Co-doped samples, the lobe of Co-Co shifted to lower k ranges (10–11 Å^{-1}), especially for $Co_{0.2}$, the resolved lobe located at (10 Å^{-1}, 2.5 Å), indicating the same sites maybe partially occupied by a lighter atom (Mn) compared with Co [53]. Moreover, the main lobes of $Co_{0.2}Cu_{0.8}MnO_y$ in Mn K-edge spectra (Fig. S3b2) were dramatically changed compared with the undoped sample but in similar positions with Co K-edge signals (Fig. S3c2), both in R- and k-space, showing similar atomic nature in the spinel structure. Based on the FT- and WT-EXAFS results, Co ions are likely located at the A and/or B sites in the spinel phase instead of copper (Cu^{2+}) or manganese (Mn^{3+}) ions. For $Co_{0.2}Cu_{0.8}MnO_y$, the located sites of Co were the same as Mn sites.

Fig. 3 shows the normalized XANES spectra and the corresponding first-order derivatives of the catalysts and references samples. The first-order derivatives were carried out to confirm further the average oxidation state (AOS) of the transition metals by XANES spectra according to the linear relationship between AOS and adsorption edge (E_0) [54]. The Cu K-edge XANES spectra (Fig. 3a) of the $Co_xCu_{1-x}MnO_y$ were

similar to the reference CuO. Moreover, the E_0 value of $Co_xCu_{1-x}MnO_y$ was around 8983.3 eV (Fig. 3b), which was also the same as that of CuO, suggesting that Cu mainly existed as Cu^{2+} in the catalysts. In the case of Mn species, the XANES spectra (Fig. 3c) of the catalysts had similar features to Mn_2O_3 and MnO_2 in the pre-edge and post-edge regions. The E_0 values of Co_0 (6548.2 eV) and other Co-doped samples (6548.9 eV) were located between Mn_2O_3 (6547.8 eV) and MnO_2 (6550.0 eV), as shown in Fig. 3d, revealing that the Mn in catalysts were primarily composed of Mn^{3+} with a small amount of Mn^{4+}, and the concentration of Mn^{4+} in Co-doped samples was higher than that of pristine Cu-Mn oxides. For the Co K-edge patterns, the peaks (shoulder, white line, and pre-peak) in XANES spectra were at similar energies to Co_3O_4 (Fig. 3e). The E_0 value of Co species in $Co_xCu_{1-x}MnO_y$ (x = 0.4–0.8) was also close to that of Co_3O_4 (7717.3 eV), while the adsorption edge of $Co_{0.2}$ (7718.0 eV) was slightly higher than that of Co_3O_4 (Fig. 3f), indicating that the content of Co^{3+} in $Co_{0.2}$ was higher than that in other Co-doped samples.

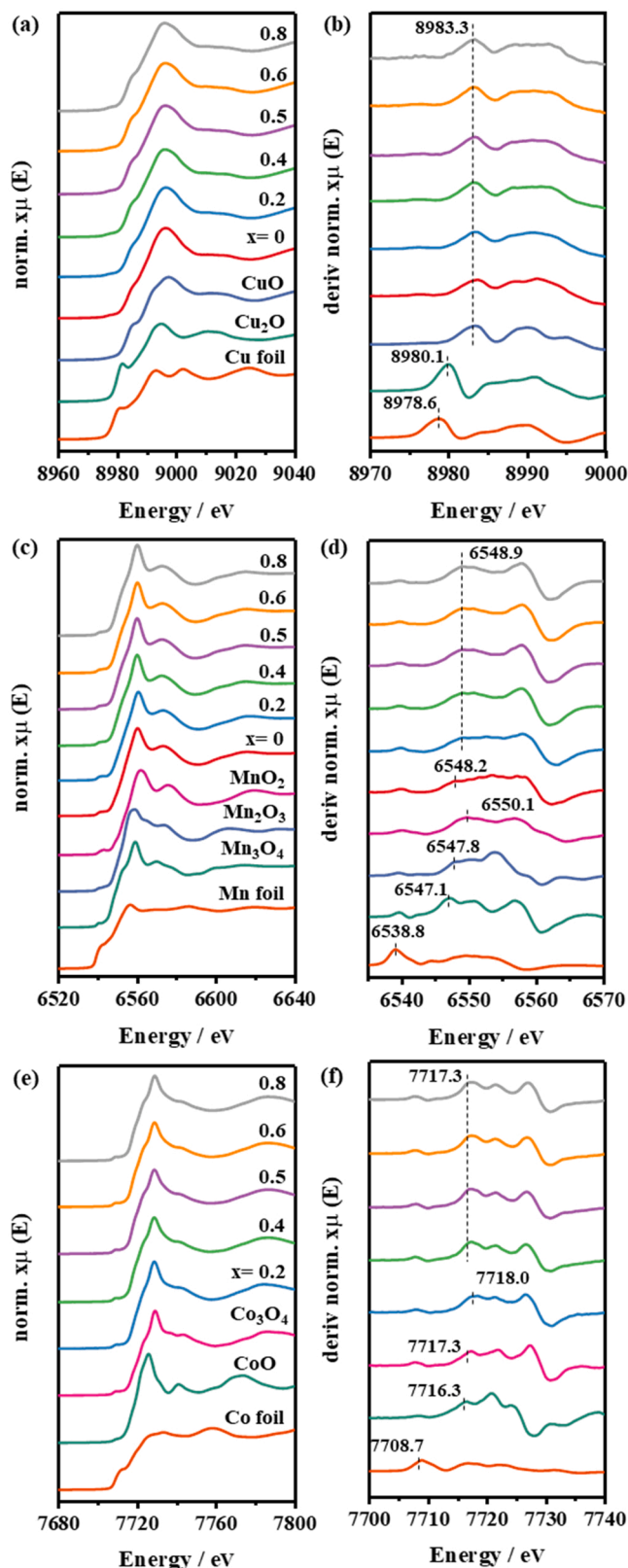**Fig. 3.** XANES spectra of $Co_xCu_{1-x}MnO_y$ and reference samples.

3.2. Surface physicochemical analysis

Temperature-programmed reduction with H_2 (H_2-TPR) was carried out to compare the oxygen reactivity and mobility of the catalysts (Fig. 4). Regarding the single oxides, one broad reduction peak in

200–350 ℃ of CuO corresponded to the transformation of CuO to Cu species. The two peaks in the range of 250–350 ℃ and 350–500 ℃ for MnO_x can be assigned to the reduction process of Mn_2O_3 to Mn_3O_4 and Mn_3O_4 to MnO, respectively. In CoO_x, the peaks in 220–330 ℃ and 330–430 ℃ correspond to the reduction of Co_2O_3/Co_3O_4 to CoO and CoO to Co, respectively. In the case of the Cu-Mn mixed oxides, the reduction occurred at rather lower temperatures (150–230, 230–260, 260–320 ℃), suggesting that the dissociation of H_2 on Cu species improved the oxygen activity of the adjacent Mn species within the spinel framework, and facilitated the reduction. The promotion effect was also shown in the 1:1 mixture of the CuO and MnO_x, but not so significant, indicating that the spinel structure was conducive to improving the reducibility of the catalysts. After Co substitution, the initial reduction temperatures decreased, indicating that the Co-substitution promoted the reactivity of the oxygen species and the low-temperature activity. Furthermore, due to the overlapped reduction peaks for each species, we assessed the reducibility of the catalysts by different temperature regions. The amount of the H_2 consumption on $Co_{0.2}$ was 3.11 mmol g^{-1} in 50–225 ℃ (Table 1), which occupied the largest proportion (27.2 %) of the total amount, suggesting the highest reactivity of the low-temperature oxygen.

Fig. 5 compares the temperature-programmed reduction profiles of the Cu-Mn and Co-doped Cu-Mn catalysts with benzene (benzene-TPR). A control experiment without packing catalysts into the reactor was performed under the same conditions (Fig. S4). It confirmed that benzene pyrolysis did not proceed without catalysts under our conditions. As the temperature increased, benzene decomposition and CO_2 generation started at around 257 ℃ on $CuMnO_x$ (Fig. 5a) and 106 ℃ on $Co_{0.2}Cu_{0.8}MnO_y$ (Fig. 5b). The total amount of the oxidized benzene was 2.72×10^{-5} mol on $Co_{0.2}Cu_{0.8}MnO_y$, equal to the amount of the CO_2 formation (1.61×10^{-4}), which was 24.5 times larger than that on $CuMnO_x$. The amount of oxygen species consumed was estimated to be 4.08×10^{-4} mol and 1.67×10^{-5}, respectively. Thus, the substitution of Co increases the amount of lattice oxygen contributing to benzene oxidation and improves the reactivity of the lattice oxygen.

The benzene temperature-programmed desorption (benzene-TPD) measurements were performed to study the adsorption property and reactivity of the catalysts (Fig. 6). During the benzene pre-adsorption process, the amount of the adsorbed benzene was determined to be 3.67×10^{-4} mol for $Co_{0.2}Cu_{0.8}MnO_y$, which exhibited a more substantial adsorption property than the pristine Cu-Mn oxide (2.81×10^{-4} mol). After N_2 purging, the physically absorbed benzene was removed. In the case of the temperature-programmed process, benzene desorption was dominant in the low-temperature region generating two signal peaks at about 64 and 101 ℃ for both samples, which indicated that there were two types of strong adsorption sites for benzene. Moreover, the amount of the adsorbed benzene was more for $Co_{0.2}Cu_{0.8}MnO_y$, especially the 101 ℃ signal corresponding to stronger adsorption. CO_2 was also generated from relatively low temperatures (40 ℃ for $Co_{0.2}$ and 62 ℃ for Co_0). At higher temperatures, TPD profiles showed several peaks due to CO_2 at approximately 138, 209, and 243 °C, which can be attributed to the reaction between the surface lattice oxygen species and the strongly adsorbed benzene [55]. The CO_2 production started at a lower temperature on $Co_{0.2}Cu_{0.8}MnO_y$, and the amount of CO_2 formed was estimated to be 1.84×10^{-4} mol which was more than that of $CuMnO_x$ (1.55×10^{-4} mol), confirming that the reactivity of surface lattice oxygen was enhanced by the Co substitution.

3.3. Catalytic activity and kinetic studies

Fig. 7a shows the benzene oxidation activities of the catalysts in the temperature range of 125–250 ℃. Benzene was completely decomposed into CO_2 and H_2O at each temperature, and no C-containing byproducts were detected for all the catalysts. The single oxides exhibited quite low activities in this temperature region, in which MnO_x showed almost no activity and Co_3O_4 showed the highest activity among the single oxides
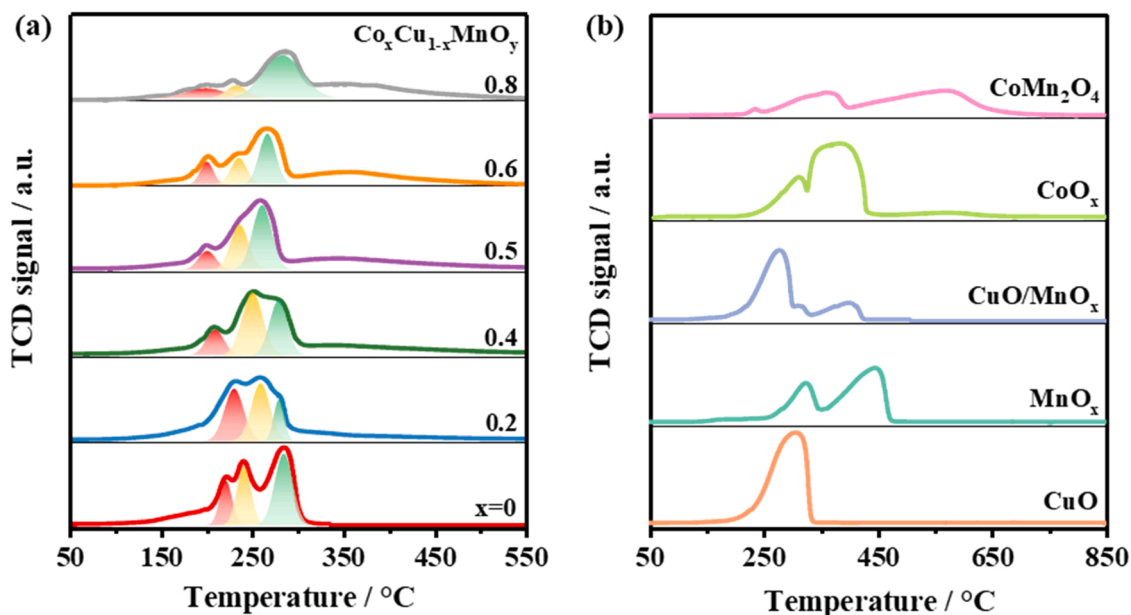
Fig. 4. H_2-TPR profiles of (a) catalysts and (b) reference samples. Catalyst weight 0.05 g, 5 % H_2-N_2 with flow rate 30 mL min^{-1}, temperature ramp 5 K min^{-1}.
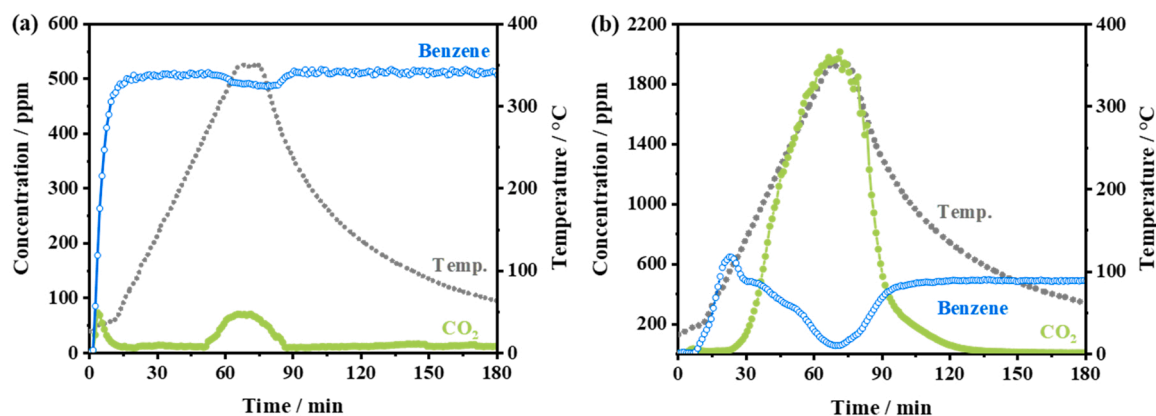

Fig. 5. Benzene-TPR profiles of (a) CuMnO$_x$ and (b) Co$_{0.2}$Cu$_{0.8}$MnO$_y$. Catalyst weight 0.05 g, 500 ppm Benzene-N_2 with flow rate 30 mL min^{-1}, temperature ramp 5 K min^{-1}. Pretreatment: purge at 300 °C in N_2 stream for 2 h.

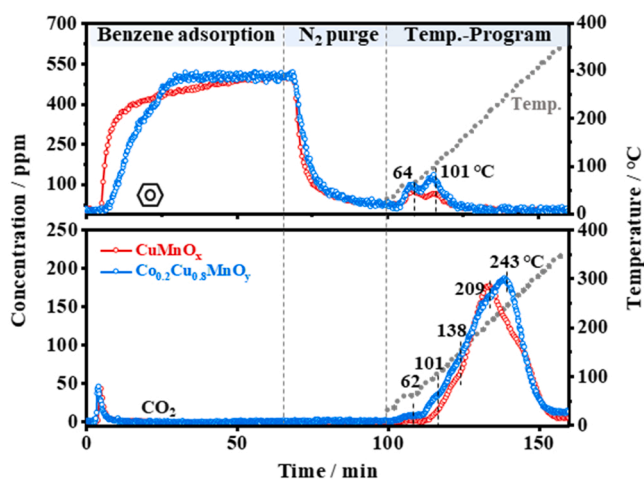**Fig. 6.** Benzene-TPD on the catalysts. Pretreatment: purge at 300 °C in N_2 stream for 2 h; TPD process: benzene adsorption for 60 min, N_2 purge for 30 min, and temperature-programmed desorption from 30 °C to 350 °C with 5 °C min^{-1}.

(Fig. S5). The spinel-type ternary oxides exhibited higher catalytic activities than the binary and single oxides; Co substitution positively affected the oxidation activity. T_{50} for Co$_x$Cu$_{1-x}$MnO$_y$ trended in an increasing order of Co$_{0.2}$ < Co$_{0.8}$ < Co$_{0.6}$ < Co$_{0.5}$–Co$_{0.4}$ < Co$_0$, while T_{90} followed the trend of Co$_{0.2}$ < Co$_{0.8}$ < Co$_{0.4}$ < Co$_{0.6}$ < Co$_{0.5}$ < Co$_0$, which was in good agreement with the reaction rate at 175 °C (Table 4). Benzene was completely oxidized on Co$_{0.2}$Cu$_{0.8}$MnO$_y$ was at 225 °C and higher temperatures, which was superior to most of the metal oxides, even slightly exceeded some noble metal catalysts when compared to previous studies in Table S2. Additionally, the stability and reproducibility of benzene oxidation reactions on Co$_{0.2}$Cu$_{0.8}$MnO$_y$ were also confirmed in Fig. S6. The benzene conversion kept stable in the long-term and 3 times cycling experiments, indicating high thermal stability of the catalyst.

The catalytic properties of Cu-Mn and Co-Cu-Mn mixed oxides were also compared with other Co-containing spinel oxides (Fig. 7a, b). The activity of CoMn$_2$O$_4$ was slightly lower than Cu-Mn oxide, indicating that the Cu-Mn spinel framework was important for the reactions. Co$_{0.2}$ exhibited the highest activity and activity normalized with the surface area due to the relatively high adsorption property and oxygen reactivity. Thus, a small amount of Co substitution into Cu-Mn oxides significantly improved the benzene oxidation activity due to the
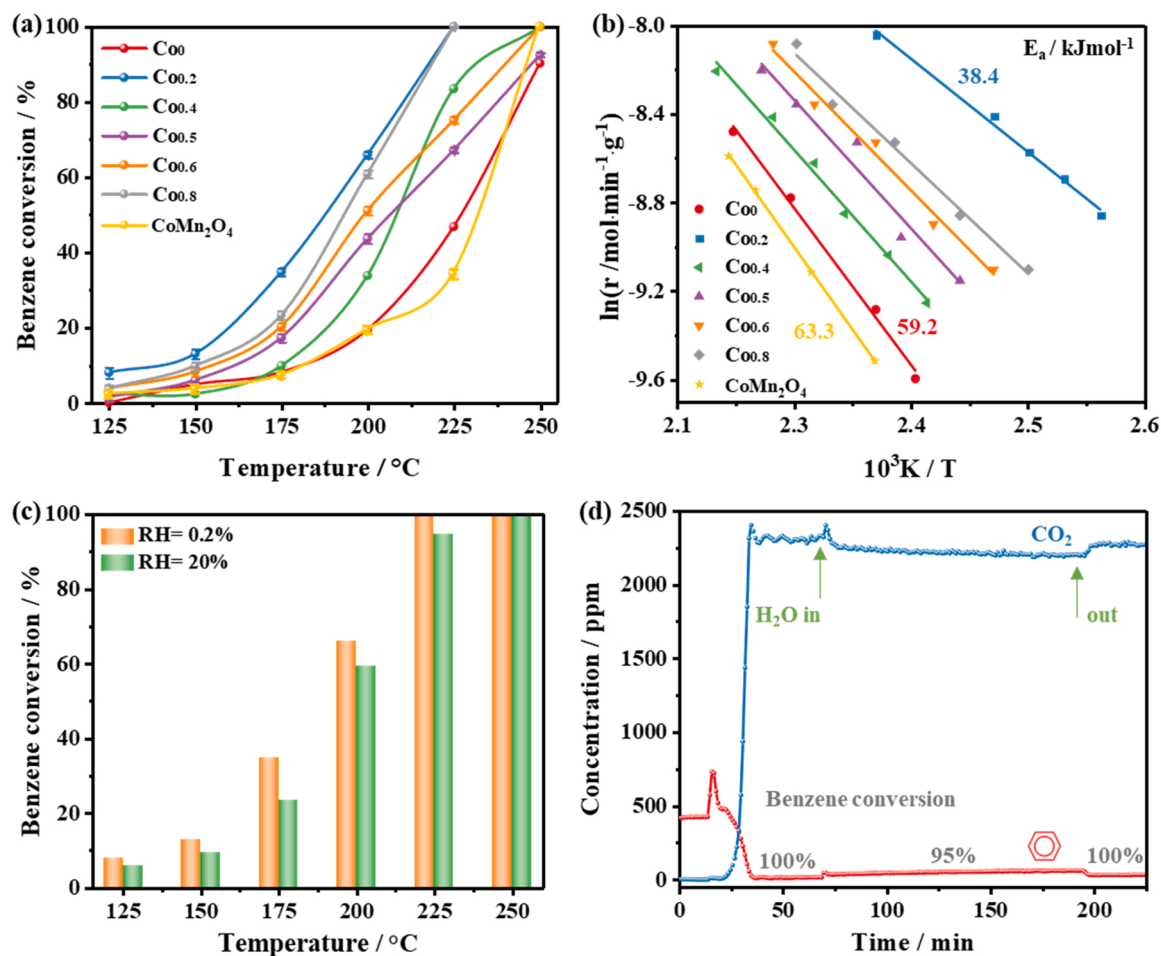
Fig. 7. (a) Benzene oxidation activities under normal conditions, (b) Arrhenius plots of the reactions, (c) activity comparison on $Co_{0.2}Cu_{0.8}MnO_y$ between dry and moisture conditions (Relative humidity, RH = 20 %), and (d) moisture stability at 225 ℃. Catalyst weight 0.10 g, benzene (400 ppm)-N_2 balance, 20 % O_2, gas flow rate 100 mL min^{-1}.

Table 4
Catalytic properties of $Co_xCu_{1-x}MnO_y$.

$Co_xCu_{1-x}MnO_y$	T_{50}[a]	T_{90}[a]	Rate/$\times 10^{-4}$ mol min^{-1} g^{-1}[b]	Normalized rate by $S_{BET}/\times 10^{-6}$ mol min^{-1} m^{-2}[b]	[c]Ea/ kJ mol^{-1}
Co_0	227	250	1.45	5.23	59.2
$Co_{0.2}$	188	217	5.88	10.37	38.4
$Co_{0.4}$	209	230	1.66	3.58	49.5
$Co_{0.5}$	206	247	2.92	5.07	48.2
$Co_{0.6}$	198	240	3.43	5.24	44.6
$Co_{0.8}$	193	219	3.94	5.44	41.4

[a] T_X is denoted as the temperature at conversion of X%.
[b] Catalyst weight 0.10 g; benzene (400 ppm)-N_2 balance, 20 % O_2; gas flow rate 100 mL min^{-1}; reaction temperature 175 ℃.
[c] Arrhenius equation:

$$lnr = lnA - E_a/RT \qquad (5)$$

where r is the reaction rate, mol min^{-1} g^{-1}; A refers to the pre-exponential factor, mol min^{-1} g^{-1}; R is the gas constant, generally considered to be 8.314 J mol^{-1} K^{-1}.

enhanced lattice oxygen reactivity and benzene adsorption ability (Figs. 4 and 5). The apparent activation energy (Ea) was evaluated from the Arrhenius plot [57] (Fig. 7b), where E_a was regarded as a constant independent of temperature is summarized in Table 4. $Co_{0.2}$ showed the lowest E_a value, indicating that benzene was more easily activated and decomposed on the catalyst surface of $Co_{0.2}Cu_{0.8}MnO_y$.

Fig. 7c and d show the effect of 20 % water vapor steam on the catalytic performance and the stability test. At lower temperatures, the inhibition effect of water vapor became obvious, whereas only a slight decrease in conversion from 100 % to 94.6 % when the temperature reached 225 ℃. Furthermore, benzene removal efficiency stayed 94–95 % for 2 h on-steam reactions at 225 ℃, and the conversion recovered to 100 % quickly when the water vapor was cut off. There was almost no activity suppression at temperatures higher than 250 ℃, indicating that the benzene oxidation activity of $Co_{0.2}$ was stable under humid conditions.

3.4. In situ FTIR studies

Since the reaction mechanism and active sites of the Co-Cu-Mn-O was the same, *in situ* FTIR experiments on $Co_{0.2}$ as a typical sample were performed to detect the pathway (intermediates) in benzene oxidation on the catalysts. Fig. 8a shows the *in situ* FTIR spectra during benzene adsorption at 40 ℃ in the absence of O_2. The bands at 1580 and 1508 cm^{-1} corresponded to the vibration of the aromatic ring of benzene. The strong bands at 1557, 1542, and 1421 cm^{-1} were attributed to the carboxylate species, where the 1557 cm^{-1} band corresponded to the asymmetric –COO^- stretching vibration and the band at 1421 cm^{-1} is the symmetric –COO^- stretching vibration [55,56]. The band at 1308 cm^{-1} may be the characteristic of the anhydride species [55]. In the benzene adsorption at 150 ℃, the bands at 1565, 1558, 1538, and 1415 cm^{-1} attributed to the carboxylate species also appeared (Fig. 8b), and the
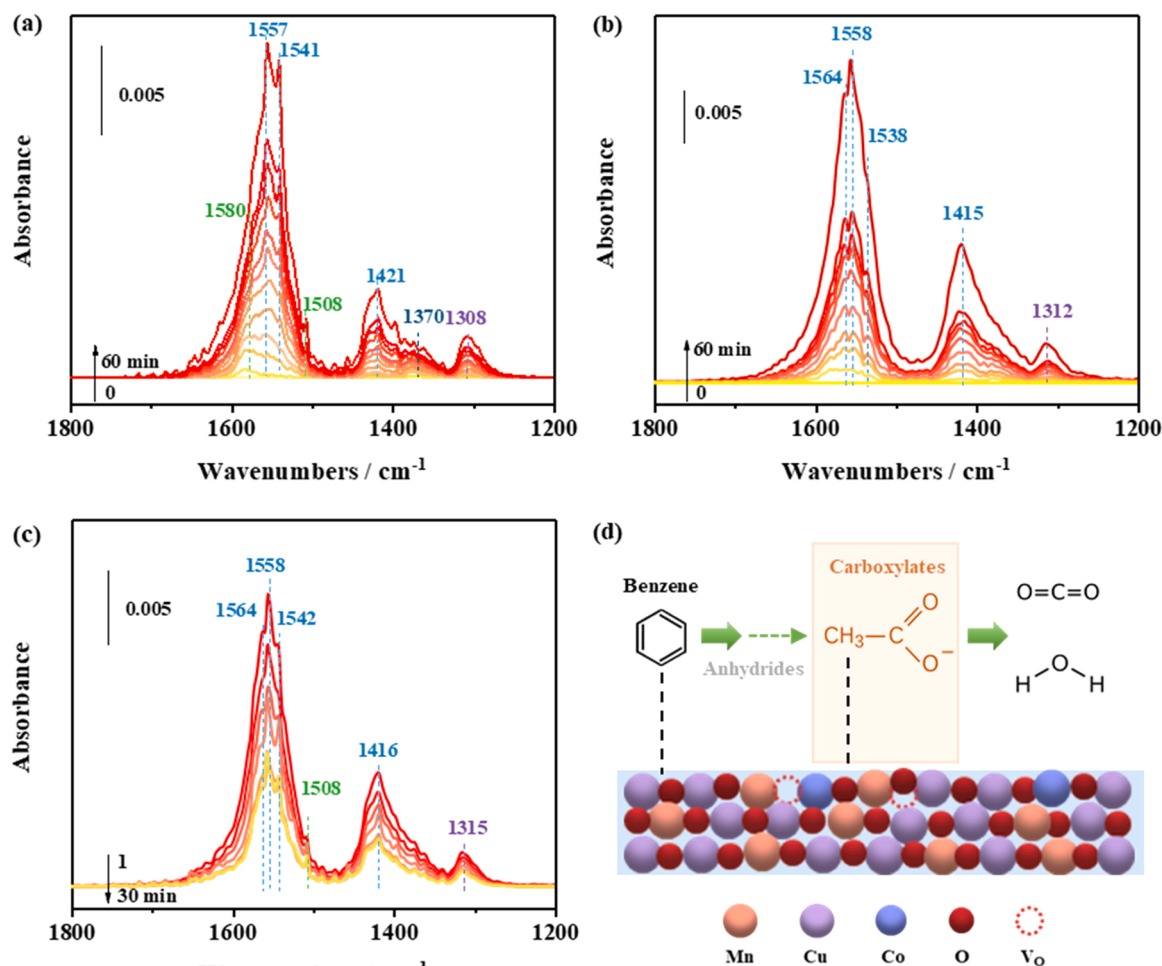
Fig. 8. *In situ* FTIR study on $Co_{0.2}Cu_{0.8}MnO_y$: (a) benzene adsorption at 150 ℃ (500 ppm benzene-N_2 balance, gas flow rate 30 mL min^{-1}), (b) introduce 20 % O_2-N_2 on the benzene-preadsorbed surface after N_2 purging at 150 ℃ (gas flow rate 30 mL min^{-1}).

intensities were stronger than that at 40 ℃. The band intensity at 1315 cm^{-1} of anhydrides was similar to spectra at 40 ℃. The bands belonging to ring vibration (1580 and 1508 cm^{-1}) disappeared. The formation of the carboxylate and anhydride species confirmed that the ring cleavage proceeded at a relatively low temperature. The intensity of the bands progressively increased with time on stream, indicating the organic products formed and accumulated on the catalyst surface. According to the *in situ* FTIR results, carboxylates were the primarily intermediate species in the absence of O_2, suggesting that lattice oxygen played a significant role in forming the carboxylate species.

In the benzene oxidation in the 20 % O_2-N_2 stream, the bands at 1564, 1558, 1542, 1416, and 1315 cm^{-1} also existed in the spectra. However, the band intensities for carboxylates decreased, suggesting that they were quickly oxidized by replenished O_2 to generate CO_2 and H_2O as final products (Fig. 8c). Thus, there is a pathway for the benzene ring to be oxidatively cleaved by surface lattice oxygen to form intermediate compounds, carboxylates and anhydrides, which are readily oxidized to CO_2 and H_2O (Fig. 8d).

3.5. Theoretical calculations

In heterogeneous catalytic oxidation of VOCs, reactants are adsorbed and activated on solid surfaces and decomposed. Our previous work has proved that benzene oxidation on Cu-Mn spinel oxides was induced by the Mars-van-Krevelen mechanism, where adsorbed benzene molecules were oxidized by surface lattice oxygen, and then the resulting oxygen vacancies were subsequently replenished by gaseous O_2 [35]. DFT

calculations were performed to study the role of Co in enhancing surface lattice oxygen activity, lowering benzene adsorption energy, and facilitating reoxidation by O_2 on Co-substituted surfaces.

Hence the first interest was to determine the lowest-energy adsorption configurations of benzene adsorbed on the surfaces. Figs. S7 and S8 show the possible active sites on Cu, Mn-terminated surfaces (involving four-fold Cu_a site, two kinds of four-fold Mn_a and Mn_b sites), and the benzene adsorption behavior on all sites (top, bridge, and hollow). Furthermore, for the Co-doped samples, Co mainly substituted the Mn sites as discussed above. The different Mn (Mn_a and Mn_b) sites were replaced by one cobalt atom to simulate the surface coordination environment and calculate their benzene adsorption energies (Fig. S8). For comparison, the Cu (Cu_a) site substituted surface was also investigated. The optimized adsorption configurations and energies of benzene on Cu-Mn and Co-doped surfaces as presented in Fig. 9a. In configuration 1 A, benzene was parallelly adsorbed between the Cu_a and Mn_a sites on $Cu_{1.5}Mn_{1.5}O_4$ (100) surface with equilibrium distances of 2.847 Å between C1 and Cu, and 2.852 Å between C4 and Mn atoms. Compared with other configurations (C1-Mn_a and C4-Mn_b, C1-Cu_a alone, C1-Mn_a alone, benzene hollow-Cu_a, and benzene hollow-Mn_a) on the Cu-Mn surface (Fig. S8), structure 1 A possessed the lowest adsorption energy of − 0.81 eV over the slab, indicating that benzene preferentially adsorbed on the Cu-Mn atom couple. The interaction between Cu, Mn-terminated surface, and benzene was closely associated with the synergy effect between Cu and Mn species. Structure 2A and 2B revealed the optimized adsorption configurations of benzene adsorbed at Co substituted Mn_a (distances of C1-Co and C4-Mn_b are 2.617 and 2.851 Å)
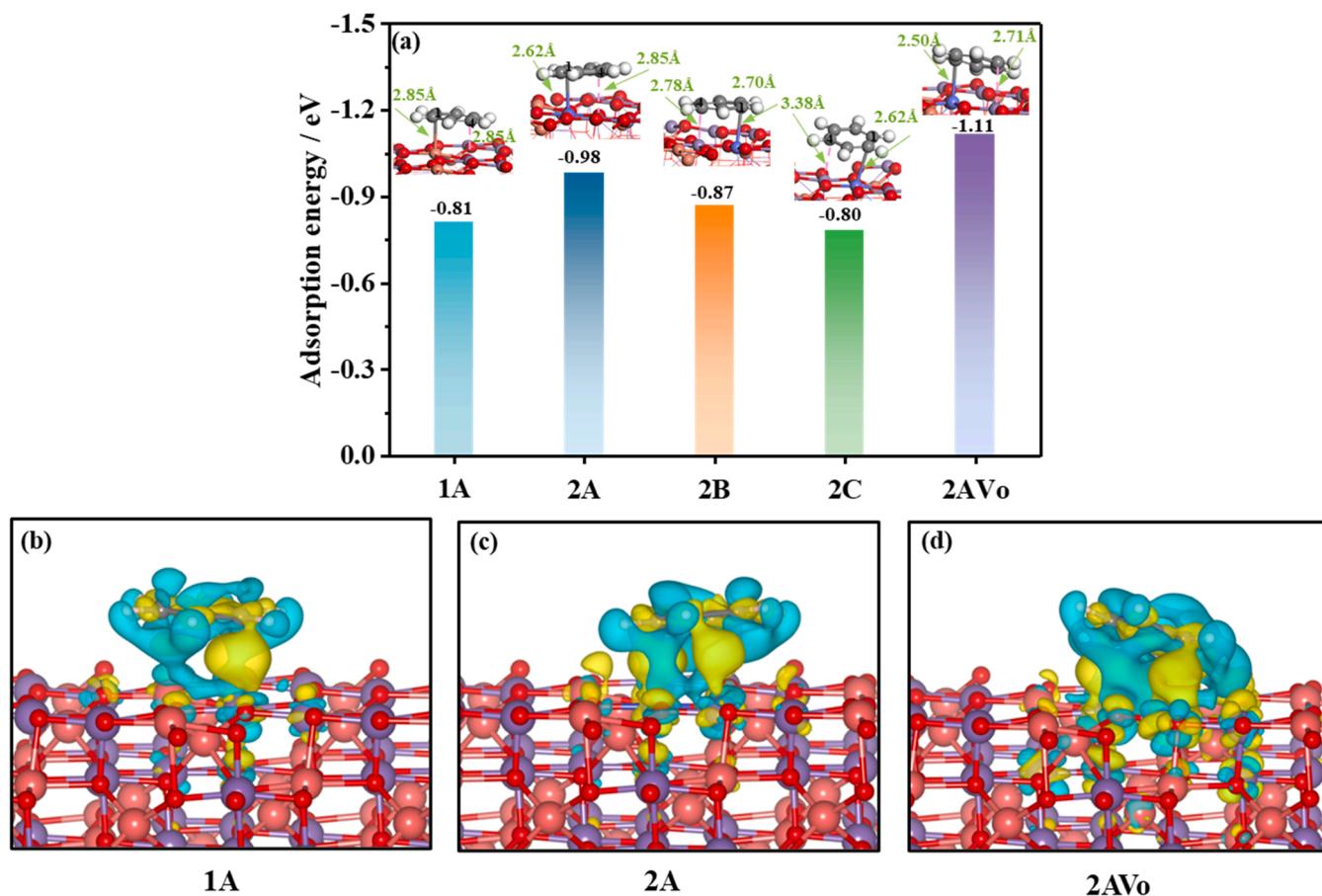
Fig. 9. (a) Benzene adsorption energy, and (b, c) charge density difference ($\delta\rho = \rho_{A+B} - \rho_A - \rho_B$) of benzene on catalyst surface. (Color scheme: Cu = pink, Mn = purple, Co = blue, O = red, C = gray, H = white).

and Mn_b (distances of C1-Co and C4-Mn_a are 2.617 and 2.851 Å) slabs, respectively. Configuration 2C showed benzene adsorbed at Co replaced Cu_a site with the distances of 2.616 Å for C1-Co, and 3.375 Å for C4-Mn_a. The adsorption energy of 2 C is − 0.78 eV lower than 2 A (− 0.98 eV) and 2B (− 0.87 eV), even slightly lower than that of 1 A (− 0.81 eV), elucidating that the Co site exhibited higher activity when co-existing with Cu and Mn species. The results agreed with the

experimental observation that Co-substitution further facilitated the catalytic activity of the Cu-Mn spinel oxides.

Based on our previous work, the apparent activation energies (E_a) of CO and benzene oxidation on Cu-Mn mixed oxides were almost identical [35]. Therefore, the activation energy of CO instead of benzene oxidation on the CuMn(100) and Co_1:CuMn(100) surfaces were calculated through transition state searching to compare the reactivity of surface
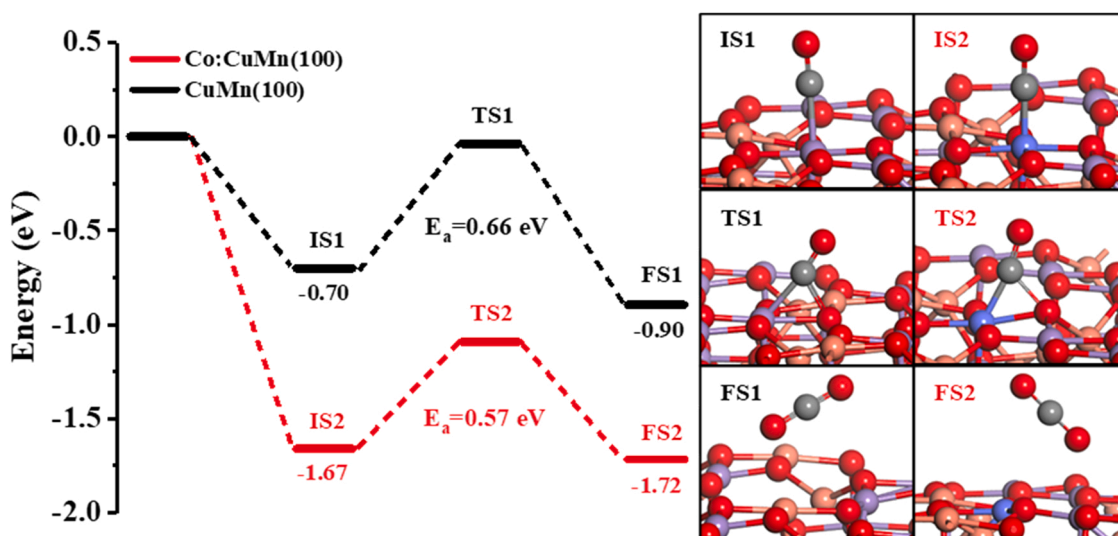

Fig. 10. Reaction energy profiles and corresponding structures for the degradation of CO on the CuMn(100) and Co:CuMn(100) surface.

lattice oxygen of the catalysts (Fig. 10). For the CO oxidation pathway, the optimum CO adsorbed on the surface was the initial state (IS), and the O-defective surface with the departed CO_2 was regarded as the final state (FS). On the CuMn(100) surface, the calculated energy barrier of CO oxidation by lattice oxygen was 0.66 eV, while that is 0.57 eV on the Co-substituted surface. The CO oxidation process was favorable on Co_1:CuMn(100) surface with highly active lattice oxygen, which was in agreement with the results of the CO oxidation activity (Fig. S9). Thus, the Co substitution facilitated the activation of the lattice oxygen for benzene decomposition. It is also worth noting that the oxygen vacancy formation energy for 4B (1.84 eV) was also slightly lower than 4A (1.89 eV) and 3A (2.12 eV), revealing the easier formation of the oxygen vacancies on the Co-replaced surface.

In addition, the generated O defect exhibited stronger adsorption and activation capacity for benzene (− 1.11 eV), which also elucidated that benzene adsorption can promote the formation of oxygen vacancies. The differential charge density of configurations 1A, 2A, and 2AVo, highlighting the regions of electron density depletion and accumulation, were also investigated to predict the interaction strength between benzene and the surfaces, as illustrated in Fig. 10 (b–d). It demonstrated the charge transfer between Cu/Co, Mn, and benzene, and the Co-doped surface exhibited stronger interaction and more electron transfer at

the interface. In the case of adsorption at the Vo site, the charge transfers between C and H atoms of benzene were more abundant, suggesting that the formation of oxygen vacancies can facilitate benzene adsorption and activation.

Fig. 11a shows the optimized adsorption configurations of oxygen molecules absorbed at the V_O site on the CuMn(100) and Co_1:CuMn (100) (Mn_a-substituted slab) surfaces. In structure 3 A, O_2 adsorbed at the Vo site between Cu and Mn atoms on CuMn(100), forming an interatomic distance of 2.005 Å for Cu–O and 2.114 Å for Mn-O, releasing adsorption energy of − 1.80 eV. Optimized O—O bond in the O_2 molecule was lengthened to 1.429 Å. Configurations 4 A and 4B represented O_2 adsorbed at the single O defect between Cu and Mn, Co and Mn atoms on Co_1:CuMn(100) surface, respectively, and their adsorption stability followed the order 4B (− 2.14 eV) > 4A (− 1.62 eV). In configuration 4B, the O_2 molecule strongly adsorbed at the Vo site wherein one end of O_2 bound at the Co site, and the other ended at the Mn site, terminating in the interatomic bond Co—O and Mn—O of 1.919 Å and 2.031 Å, respectively. The O—O bond was stretched to 1.432 Å from around 1.23 Å of original molecular oxygen, which was close to the O_2^- (1.33 Å) and O_2^{2-} (1.44 Å) [58,59]. The weaker O—O bonds suggested that the peroxo (O_2^{2-}) and superoxide (O_2^-) species were likely precursors for O_2 dissociation and replenishment into the
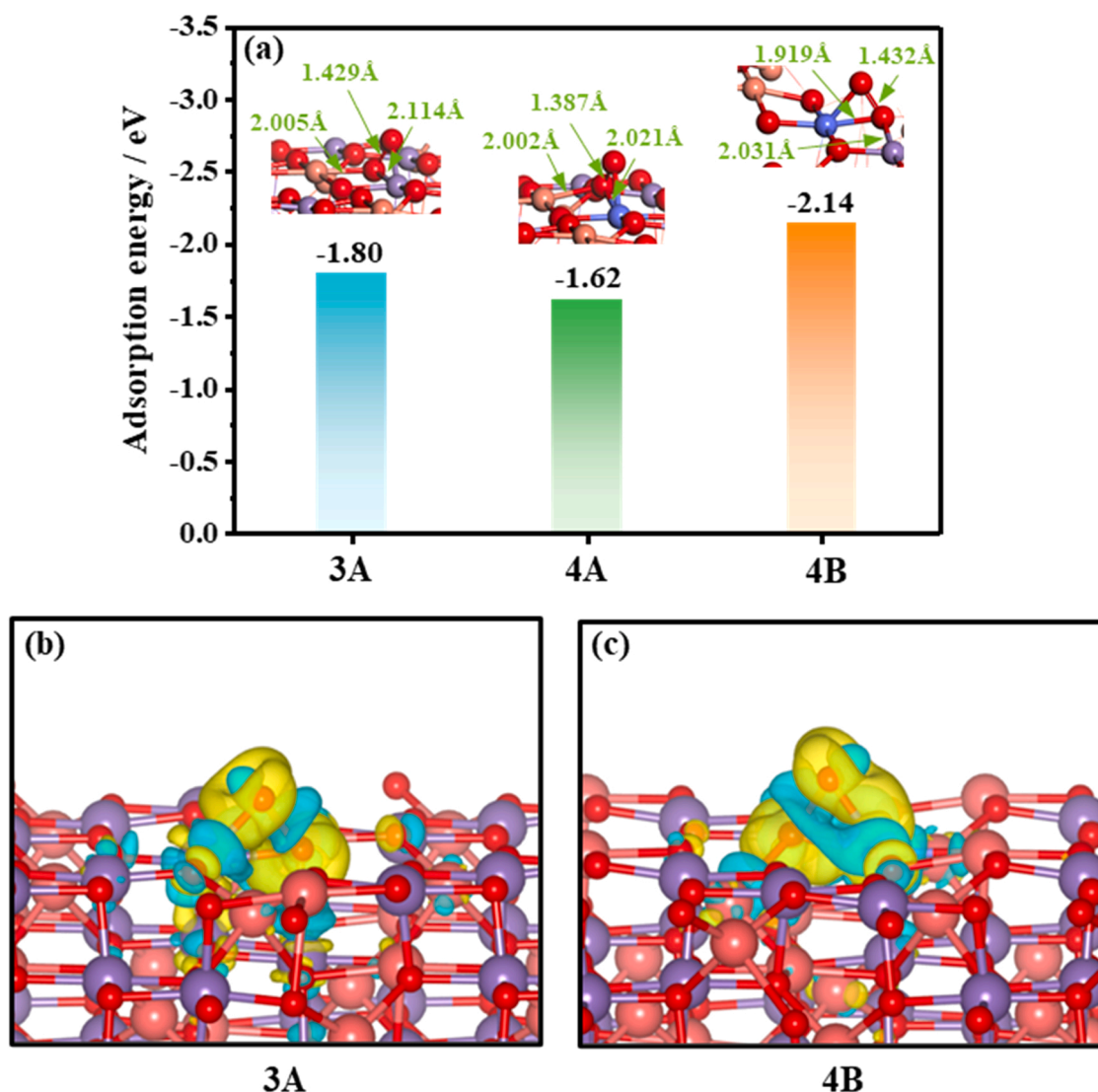
Fig. 11. DFT simulations: (a) O_2 adsorption energy, and (b, c) charge density difference (($\delta\rho = \rho_{A+B} - \rho_A - \rho_B$) of adsorbed O_2 at Vo site. (Color scheme: Cu = pink, Mn = purple, Co = blue, O = red).

surfaces. For further insight into the effect of the interaction of oxygen and the slabs, differential charge density isosurface contours, providing electron density redistribution after adsorption, were shown in Fig. 11b and c. The adsorbed O_2 was polarized at the Vo site, and charge transferred from interacting metal ions to O_2 was demonstrated, whereas the Co-doped surface was stronger than the undoped one.

Furthermore, to investigate the effect of Co substitution, the benzene adsorption on dual and triple Co-substituted surfaces and the O_2 adsorption on the corresponding active Vo sites were configured in Fig. 12. The lowest-energy configurations of adsorbed benzene on the surface of 5A-Co_2:CuMn(100) and 6A-Co_3:CuMn(100) were one C (C1) atom in benzene molecule coordinated with Cu site and the opposite C (C4) atom ended at the Co site, which was not similar to that on 3A-Co_1:CuMn(100). The adsorption energies of configurations 3A, 5A, and 6A were − 0.983, − 0.924, and − 0.926 eV, respectively. The adsorption configurations of benzene bonding with different Co sites were also calculated in Figs. S10 and S11, revealing that benzene tended to adsorb around the first Co site on the surfaces. O_2 adsorption energies on the single O defect of surfaces 3AVo, 5AVo, and 6AVo were − 2.14, − 2.03, and − 2.08 eV. Therefore, the adsorption structure on the Co_1:CuMn (100) slab was the strongest.

For the H_2O–Co_1:CuMn(100) interactions (Fig. 13a), the water molecule was found to bind preferentially at the Co site *via* the O atom with the interacting O–Co distance of 2.007, releasing adsorption energy of − 1.20 eV. The stronger binding suggested that the competitive adsorption between water vapor and benzene (− 0.98 eV) on Co sites was one of the reasons for deactivation under moisture conditions. The adsorptions on Cu (− 0.39 to − 0.42 eV) and Mn (− 0.83 to − 1.02 eV) sites were weaker than on Co sites (Fig. S12), suggesting H_2O energetically preferred adsorbing on Co rather than Co-Mn or Co-Cu bridge sites. However, the adsorption mode of benzene was not ending on only the Co site but interacting with Co-Mn-Cu (Fig. S13), which revealed that the adsorbed H_2O did not completely cover the active site and prevent the activation of benzene. Fig. 13b shows the optimized configuration of H_2O adsorption at the Vo site·H_2O interacted with Co, Cu, and Mn atoms releasing adsorption energy of − 0.90 eV, much lower than O_2 adsorption (− 2.14 eV). Investigation of the H_2O adsorption at the Vo site revealed that compared to obstructing the benzene activation, the water vapor less affected dissociation and replenishment of O_2. Therefore, the existence of water vapor did not significantly inhibit the benzene oxidation efficiency.

4. Conclusion

In this work, catalytic oxidation of benzene has been efficiently proceeded over Co-substituted Cu-Mn mixed oxides. The effect of Co addition on the physicochemical properties and catalytic behavior was studied in detail by experimental and theoretical analysis. The formation of the spinel phase and the substitution of Mn sites in Cu-Mn oxides by Co species were characterized by XRD and XAFS spectra (Fourier and
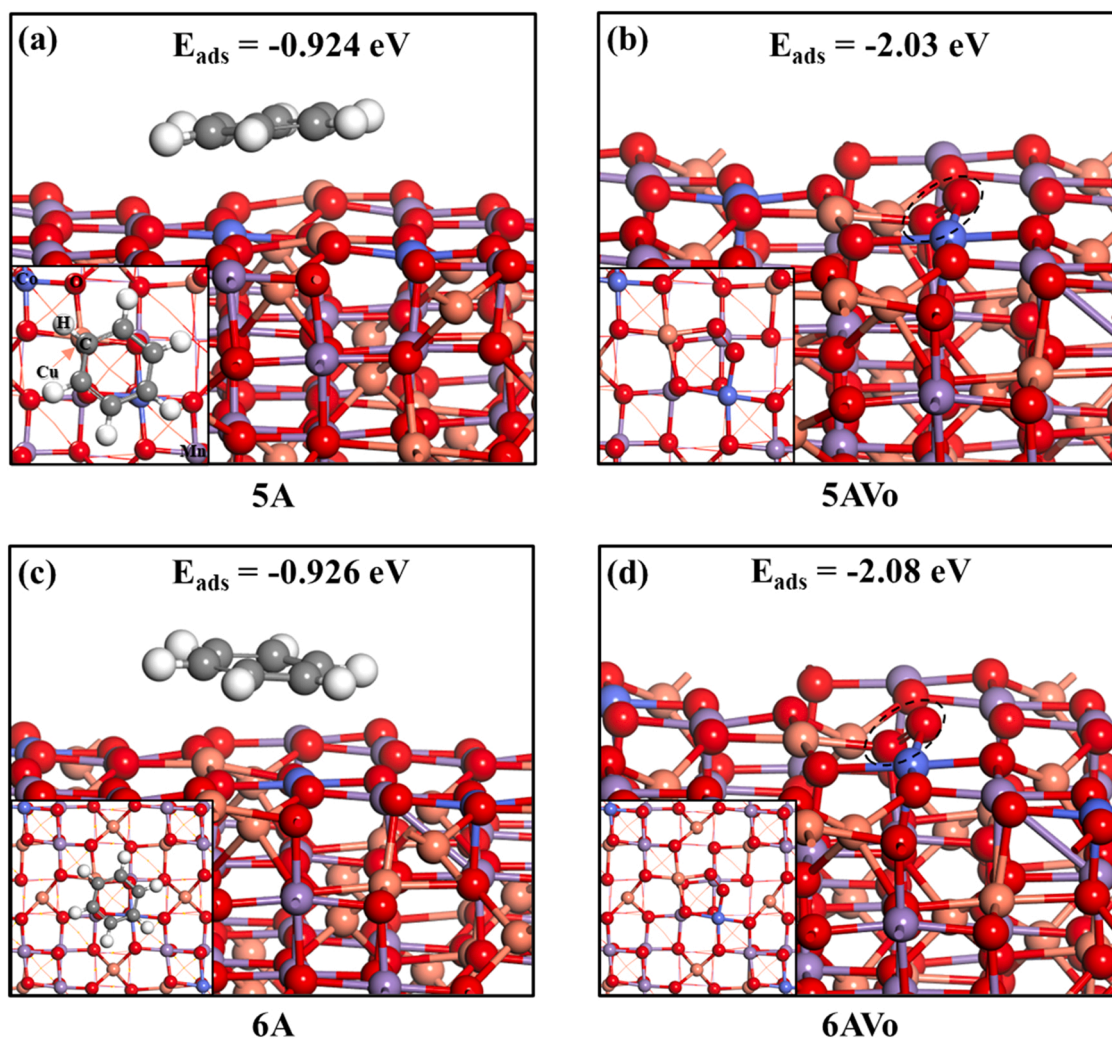
Fig. 12. Adsorption configurations and energies of benzene on (a) dual and (c) triple Co-substituted Cu-Mn (100) surface, and (b, d) O_2 at corresponding Vo site, respectively. (Color scheme: Cu = pink, Mn = purple, Co = blue, O = red, C = gray, H = white).
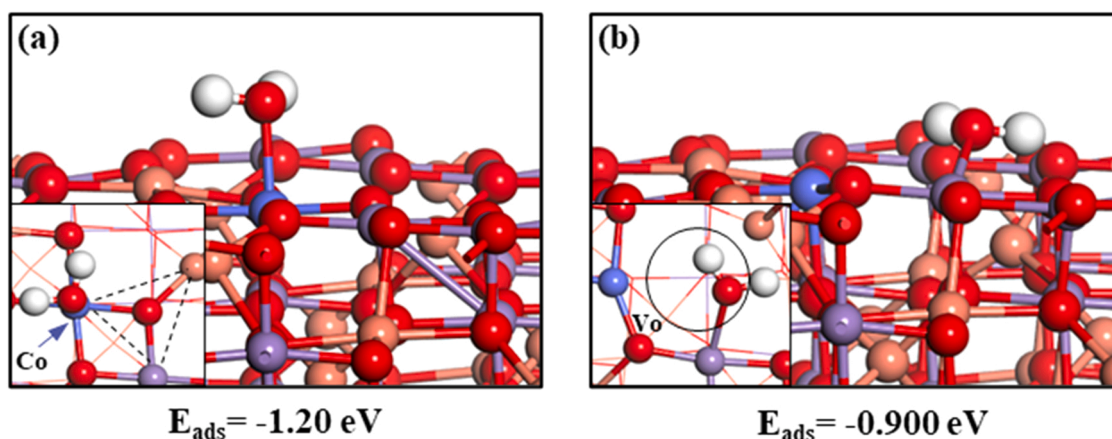
Fig. 13. Adsorption configurations and energies of H_2O molecule on (a) slab and (b) Vo site. (Color scheme: Cu = pink, Mn = purple, Co = blue, O = red, H = white).

Wavelet transformed EXAFS and XANES). *In situ* FTIR studies revealed that carboxylates and anhydrides were formed on the catalysts surface, which were readily oxidized to CO_2. Compared with the single and Cu-Mn mixed oxide, the Co-doped catalysts showed significantly higher benzene oxidation activities due to the enhanced reactivity of lattice oxygen species, the increased specific surface area, and the improved chemisorption of benzene. Furthermore, this mode can also be applied to humid conditions with high activity and stability. The effect of Co substitution took multiple parts in the reactions by DFT calculations: (1) Compared with the Cu-Mn surface, Co substituted slab was much stronger for benzene adsorption and had more active lattice oxygen. The activated benzene was reacted with lattice oxygen, and benzene was adsorbed on the generated O-defect to form more active benzene species; (2) Co-substituted Cu-Mn slab showed lower energy for oxygen vacancy formation and promoted the O_2 adsorption, dissociation, and replenishment into the lattice; (3) The H_2O molecules were more likely to bind to Co sites and did not completely cover the active site for benzene adsorption. These findings could provide a deep understanding of the effect of Co substitution on conducting highly efficient oxidation catalysts and a facile and effective strategy for improving the catalytic properties of VOC removal.

CRediT authorship contribution statement

Siyu Ding: Investigation, Formal analysis, Data curation, Theoretical calculation, Writing – original draft. **Chen Zhu:** Theoretical calculation. **Hajime Hojo:** Methodology, Supervision. **Hisahiro Einaga:** Supervision, Data interpretation, Manuscript preparation.

Declaration of Competing Interest

The authors declare that they have no known competing financial interests or personal relationships that could have appeared to influence the work reported in this paper.

Data Availability

Data will be made available on request.

Acknowledgments

Appendix A. Supporting information

Supplementary data associated with this article can be found in the online version at doi:10.1016/j.apcatb.2022.122099.

References

[1] S. Dolai, S.K. Bhunia, S.S. Beglaryan, S. Kolusheva, L. Zeiri, R. Jelinek, Colorimetric polydiacetylene–aerogel detector for volatile organic compounds (VOCs), ACS Appl. Mater. Interfaces 9 (2017) 2891–2898.
[2] C. Domeño, Á. Rodríguez-Lafuente, J. Martos, R. Bilbao, C. Nerín, VOC removal and deodorization of effluent gases from an industrial plant by photo-oxidation, chemical oxidation, and ozonization, Environ. Sci. Technol., vol. 44, 200, pp. 2585–91.
[3] D. Li, X. Chen, C. Shu, Y. Huang, P. Zhang, Bi Xiao, D. Zhou, Ca-decorated MoBOH as a promising adsorbent for CH_2O, C_6H_6, C_3H_6O, and C_2HCl_3 removal at room temperature: a first-principle study, Appl. Surf. Sci. 563 (2021), 150233.
[4] G. Zhang, X. Huang, Z. Tang, Enhancing water resistance of a Mn-based catalyst for low temperature selective catalytic reduction reaction by modifying super hydrophobic layers, ACS Appl. Mater. Interfaces 11 (2019) 36598–36606.
[5] S. Arriaga, R. Muñoz, S. Hernandez, B. Guieysse, S. Revah, Gaseous hexane biodegradation by fusarium solani in two liquid phase packed-bed and stirred-tank bioreactors, Environ. Sci. Technol. 40 (2006) 2390–2395.
[6] E. Dumont, G. Darracq, A. Couvert, C. Couriol, A. Amrane, D. Thomas, Y. Andrès, P. Le, Cloirec, volumetric mass transfer coefficients characterising VOC absorption in water/silicone oil mixtures, Chem. Eng. J. 221 (2013) 308–314.
[7] S. Cao, X. Fei, Y. Wen, Z. Sun, H. Wang, Z. Wu, Bimodal mesoporous TiO_2 supported Pt, Pd and Ru catalysts and their catalytic performance and deactivation mechanism for catalytic combustion of dichloromethane (CH_2Cl_2), Appl. Catal. A: Gen. 550 (2018) 20–27.
[8] L. Wang, M. Sakurai, H. Kameyama, Catalytic oxidation of dichloromethane and toluene over platinum alumite catalyst, J. Hazard. Mater. 154 (2008) 390–395.
[9] B. Darif, S. Ojala, M. Kärkkäinen, S. Pronier, T. Maunula, R. Brahmi, R.L. Keiski, Study on sulfur deactivation of catalysts for DMDS oxidation, Appl. Catal. B: Environ. 206 (2017) 653–665.
[10] S. Zhang, X. Li, B. Chen, X. Zhu, C. Shi, A. Zhu, CO oxidation activity at room temperature over Au/CeO_2 catalysts: disclosure of induction period and humidity Effect, ACS Catal. 4 (2014) 3481–3489.
[11] J. Gao, C. Jia, L. Zhang, H. Wang, Y. Yang, S. Hung, Y. Hsu, B. Liu, Tuning chemical bonding of MnO_2 through transition-metal doping for enhanced CO oxidation, J. Catal. 341 (2016) 72–81.
[12] S. Rong, P. Zhang, F. Liu, Y. Yang, Engineering crystal facet of α-MnO_2 nanowire for highly efficient catalytic oxidation of carcinogenic airborne formaldehyde, ACS Catal. 8 (2018) 3435–3446.
[13] L. Li, Q. Yang, D. Wang, Y. Peng, J. Yan, J. Li, J. Crittenden, Facile synthesis λ-MnO_2 spinel for highly effective catalytic oxidation of benzene, Chem. Eng. J. 421 (2021), 127828.
[14] M. Li, F. Bi, Y. Xu, P. Hao, K. Xiang, Y. Zhang, S. Chen, J. Guo, X. Guo, W. Ding, Effect of residual chlorine on the catalytic performance of Co_3O_4 for CO oxidation, ACS Catal. 9 (2019) 11676–11684.
[15] J. Bae, D. Shin, H. Jeong, C. Choe, Y. Choi, J.W. Han, H. Lee, Facet-dependent Mn doping on shaped Co_3O_4 crystals for catalytic oxidation, ACS Catal. 11 (2021) 11066–11074.
[16] S. Carlos-Cuellar, P. Li, A.P. Christensen, B.J. Krueger, C. Burrichter, V.H. Grassian, Heterogeneous uptake kinetics of volatile organic compounds on oxide surfaces using a Knudsen cell reactor: adsorption of acetic acid, formaldehyde, and methanol on α-Fe_2O_3, α-Al_2O_3, and SiO_2, J. Phys. Chem. A 107 (2003) 4250–4261.

[17] Y. Zeng, Y. Wang, F. Song, S. Zhang, Q. Zhong, The effect of CuO loading on different method prepared CeO$_2$ catalyst for toluene oxidation, Sci. Total Environ. 712 (2020), 135635.

[18] Q. Dai, Z. Zhang, J. Yan, J. Wu, G. Johnson, W. Sun, X. Wang, S. Zhang, W. Zhan, Phosphate-functionalized CeO$_2$ nanosheets for efficient catalytic oxidation of dichloromethane, Environ. Sci. Technol. 52 (2018) 13430–13437.

[19] Z. Su, W. Yang, C. Wang, S. Xiong, X. Cao, Y. Peng, W. Si, Y. Weng, M. Xue, J. Li, Roles of oxygen vacancies in the bulk and surface of CeO$_2$ for toluene catalytic combustion, Environ. Sci. Technol. 54 (2020) 12684–12692.

[20] M. Morales, B. Barbero, L. Cadus, Total oxidation of ethanol and propane over Mn-Cu mixed oxide catalysts, Appl. Catal. B: Environ. 67 (2006) 229–236.

[21] M. Zimowska, A. Michalik-Zym, R. Janik, T. Machej, J. Gurgul, R.P. Socha, J. Podobiński, E.M. Serwicka, Catalytic combustion of toluene over mixed Cu–Mn oxides, Catal. Today 119 (2007) 321–326.

[22] S. Dey, G.C. Dhal, D. Mohan, R. Prasad, Effect of various metal oxides phases present in CuMnO$_x$ catalyst for selective CO oxidation, Mater. Discov. 12 (2008) 63–71.

[23] Z. Tian, P.H.T. Ngamou, V. Vannier, K. Kohse-Höinghaus, N. Bahlawane, Catalytic oxidation of VOCs over mixed Co–Mn oxides, Appl. Catal. B: Environ. 104 (2012) 125–134.

[24] D.A. Aguilera, A. Perez, R. Molina, S. Moreno, Cu–Mn and Co–Mn catalysts synthesized from hydrotalcites and their use in the oxidation of VOCs, Appl. Catal. B: Environ. 104 (2011) 144–150.

[25] J. Niu, H. Liu, Y. Zhang, X. Wang, J. Han, Z. Yue, E. Duan, NiCo$_2$O$_4$ spinel for efficient toluene oxidation: the effect of crystal plane and solvent, Chemosphere 259 (2020), 127427.

[26] D. Delimaris, T. Ioannides, VOC oxidation over MnO$_x$–CeO$_2$ catalysts prepared by a combustion method, Appl. Catal. B: Environ. 84 (2008) 303–312.

[27] H. Li, G. Qi, X. Tana, X. Zhang, W. Huang, W. Li, Shen, Low-temperature oxidation of ethanol over a Mn$_{0.6}$Ce$_{0.4}$O$_2$ mixed oxide, Appl. Catal. B: Environ. 103 (2011) 54–61.

[28] Z. Wang, G. Shen, J. Li, H. Liu, Q. Wang, Y. Chen, Catalytic removal of benzene over CeO$_2$–MnO$_x$ composite oxides prepared by hydrothermal method, Appl. Catal. B: Environ. 138–139 (2013) 253–259.

[29] L.F. Liotta, M. Ousmane, G. Di Carlo, G. Pantaleo, G. Deganello, A. Boreave, A. Giroir-Fendler, Catalytic removal of toluene over Co$_3$O$_4$–CeO$_2$ mixed oxide catalysts: comparison with Pt/Al$_2$O$_3$, Catal. Lett. 127 (2008) 270–276.

[30] L.F. Liotta, M. Ousmane, G. Di Carlo, G. Pantaleo, G. Deganello, G. Marcì, L. Retailleau, A. Giroir-Fendler, Total oxidation of propene at low temperature over Co$_3$O$_4$–CeO$_2$ mixed oxides: role of surface oxygen vacancies and bulk oxygen mobility in the catalytic activity, Appl. Catal. A: Gen. 347 (2008) 81–88.

[31] A. Aranda, E. Aylon, B. Solsona, R. Murillo, A.M. Mastral, D.R. Sellick, S. Agouram, T. Garcia, S.H. Taylor, High activity mesoporous copper doped cerium oxide catalysts for the total oxidation of polyaromatic hydrocarbon pollutants, Chem. Commun. 48 (2012) 4704–4706.

[32] Z. Zhao, X. Lin, R. Jin, G. Wang, T. Muhammad, MO$_x$ (M = Mn, Fe, Ni or Cr) improved supported Co$_3$O$_4$ catalysts on ceria–zirconia nanoparticulate for CO preferential oxidation in H$_2$-rich gases, Appl. Catal. B: Environ. 115–116 (2012) 53–62.

[33] X. Yao, Y. Xiong, W. Zou, L. Zhang, S. Wu, X. Dong, F. Gao, Y. Deng, C. Tang, Z. Chen, L. Dong, Y. Chen, Correlation between the physicochemical properties and catalytic performances of Ce$_x$Sn$_{1-x}$O$_2$ mixed oxides for NO reduction by CO, Appl. Catal. B: Environ. 144 (2014) 152–165.

[34] H. Einaga, A. Kiya, S. Yoshioka, Y. Teraoka, Catalytic properties of copper-manganese mixed oxides prepared by coprecipitation using tetramethylammonium hydroxide, Catal. Sci. Technol. 4 (2014) 3713–3722.

[35] S. Ding, C. Zhu, H. Hojo, H. Einaga, Enhanced catalytic performance of spinel-type Cu-Mn oxides for benzene oxidation under microwave irradiation, J. Hazard. Mater. 424 (2022), 127523.

[36] S. Ding, H. Hojo, H. Einaga, Microwave-assisted removal of benzene with high efficiency on cobalt modified copper-manganese spinel oxides, J. Environ. Chem. Eng. 10 (2022), 108212.

[37] B.X. Hu, C.H. Chen, S.J. Frueh, L. Jin, R. Joesten, S.L. Suib, Removal of aqueous phenol by adsorption and oxidation with doped hydrophobic cryptomelane-type manganese oxide (K-OMS-2) nanofibers, J. Phys. Chem. C 11 (2010) 9835–9844.

[38] A. Sharma, R.K. Dutta, A. Roychowdhury, D. Das, A. Goyal, A. Kapoor, Cobalt doped CuO nanoparticles as a highly efficient heterogeneous catalyst for reduction of 4-nitrophenol to 4-aminophenol, Appl. Catal. A: Gen. 543 (2017) 257–265.

[39] L. Deng, Y. Ding, B. Duan, Y. Chen, P. Li, S. Zhu, S. Shen, Catalytic deep combustion characteristics of benzene over cobalt doped Mn-Ce solid solution catalysts at lower temperatures, Mol. Catal. 446 (2018) 72–80.

[40] X. Tang, J. Li, J. Hao, Significant enhancement of catalytic activities of manganese oxide octahedral molecular sieve by marginal amount of doping vanadium, Catal. Commun. 11 (2010) 871–875.

[41] B. Ravel, M. Newville, ATHENA, ARTEMIS, HEPHAESTUS: data analysis for X-ray absorption spectroscopy using IFEFFIT, J. Synchrotron Rad. 12 (2005) 537–541.

[42] M. Katsikini, F. Pinakidou, E.C. Paloura, J. Arvanitidis, S. Ves, U. Reinholz, E. Papadomanolaki, E. Iliopoulos, Simulation of the EXAFS and Raman spectra of In$_x$Ga$_{1-x}$N utilizing the equation of motion routine of FEFF8, J. Phys.: Conf. Ser., vol. 712, 2016, 012126.

[43] A.A. Lavrentyev, I.Y. Nikiforov, V.A. Dubeiko, B.V. Gabrelian, J.J. Rehr, The use of the FEFF8 code to calculate the XANES and electron density of states of some sulfides, J. Synchrotron Rad. 8 (2001) 288–290.

[44] H. Funke, A.C. Scheinost, M. Chukalina, Wavelet analysis of extended X-ray absorption fine structure data, Phys. Rev. B 71 (2005), 094110.

[45] H. Funke, M. Chukalina, A.C. Scheinost, A. New, FEFF-based wavelet for EXAFS data analysis, J. Synchrotron Rad. 14 (2007) 426–432.

[46] G. Kresse, J. Furthmüller, Efficient iterative schemes for ab initio total-energy calculations using a plane-wave basis set, Phys. Rev. B 54 (16) (1996) 11169–11186.

[47] J.P. Perdew, K. Burke, M. Ernzerhof, Generalized gradient approximation made simple, Phys. Rev. Lett. 77 (1996) 3865–3868.

[48] C. Zhu, S. Ding, H. Hojo, H. Einaga, Controlling diphenyl ether hydrogenolysis selectivity by tuning the Pt support and H-donors under mild conditions, ACS Catal. 11 (2021) 12661–12672.

[49] X. Yang, X. Yu, M. Jing, W. Song, J. Liu, M. Ge, Defective Mn$_x$Zr$_{1-x}$O$_2$ solid solution for the catalytic oxidation of toluene: insights into the oxygen vacancy contribution, ACS Appl. Mater. Interfaces 11 (2019) 730–739.

[50] W. Dow, Y. Wang, T. Huang, TPR and XRD studies of yttria-doped ceria/γ-alumina-supported copper oxide catalyst, Appl. Catal. A: Gen. 190 (2000) 25–34.

[51] M. Ma, Z. Pan, W. Wang, L. Guo, J. Li, Z. Wu, S. Yang, Microstructure and gas-sensing property of the ordered mesoporous Co$_3$O$_4$, J. Nanosci. Nanotechnol. 13 (2013) 864–868.

[52] X. Wang, M. Zhu, D.L. Koopal, W. Li, W. Xu, F. Liu, J. Zhang, Q. Liu, X. Feng, D. L. Sparks, Effects of crystallite size on the structure and magnetism of ferrihydrite, Environ. Sci.: Nano 3 (2016) 190–202.

[53] V.L. Sushkevich, O.V. Safonova, D. Palagin, M.A. Newton, J.A.V. Bokhoven, Structure of copper sites in zeolites examined by Fourier and wavelet transform analysis of EXAFS, Chem. Sci. 11 (2020) 5299–5312.

[54] T. Ressler, J. Wong, J. Roos, I.L. Smith, Quantitative speciation of Mn-bearing particulates emitted from autos burning (methylcyclopentadienyl) manganese tricarbonyl-added gasolines using XANES spectroscopy, Environ. Sci. Technol. 34 (2000) 950–958.

[55] C. Dong, Z. Qu, Y. Qin, Q. Fu, H. Sun, X. Duan, Revealing the highly catalytic performance of spinel CoMn$_2$O$_4$ for toluene oxidation: involvement and replenishment of oxygen species using in situ designed-TP techniques, ACS Catal. 9 (2019) 6698–6710.

[56] X. Wang, Y. Liu, T. Zhang, Y. Luo, Z. Lan, K. Zhang, J. Zuo, L. Jiang, R. Wang, Geometrical-site-dependent catalytic activity of ordered mesoporous Co-based spinel for benzene oxidation: in situ DRIFTS study coupled with Raman and XAFS spectroscopy, ACS Catal. 7 (2017) 1626–1636.

[57] Y. Zheng, Q. Liu, C.P. Shan, Y. Su, K. Fu, S. Lu, R. Han, C. Song, N. Ji, D. Ma, Defective ultrafine MnO$_x$ nanoparticles confined within a carbon matrix for low-temperature oxidation of volatile organic compounds, Environ. Sci. Technol. 55 (2021) 5403–5411.

[58] P.H. Sit, M.H. Cohen, A. Selloni, Interaction of oxygen and water with the (100) surface of pyrite: mechanism of sulfur oxidation, J. Phys. Chem. Lett. 3 (2012) 2409–2414.

[59] U. Aschauer, J. Chen, A. Selloni, Peroxide and superoxide states of adsorbed O$_2$ on anatase TiO$_2$ (101) with subsurface defects, Phys. Chem. Chem. Phys. 12 (2010) 12956–12960.